Journal of Geophysical Research: Space Physics

RESEARCH ARTICLE
10.1029/2018JA025867

Magnetotail Configuration During a Steady Convection Event as Observed by Low-Altitude and Magnetospheric Spacecraft

V. A. Sergeev[1], N. A. Tsyganenko[1], V. Angelopoulos[2], A. V. Runov[2], and H. J. Singer[3]

[1]Earth's Physics Department, Saint-Petersburg State University, St. Petersburg, Russia, [2]Department of Earth, Planetary, and Space Sciences and Institute of Geophysics and Planetary Physics, University of California, Los Angeles, CA, USA, [3]NOAA Space Weather Prediction Center, Boulder, CO, USA

Key Points:
- Magnetotail observations and remote sensing from low altitudes are used to monitor magnetic configuration for long steady convection event
- Existing models fail to predict hybrid configuration (stretched inner tail and dipolarized midtail) formed after 3 hr of intense driving
- Unusual azimuthal current sheet in the return convection region was sporadically modulated by earthward convecting plasma structures

Supporting Information:
- Supporting Information S1

Correspondence to:
V. A. Sergeev,
victor@geo.phys.spbu.ru

Citation:
Sergeev, V. A., Tsyganenko, N. A., Angelopoulos, V., Runov, A. V., & Singer, H. J. (2018). Magnetotail configuration during a steady convection event as observed by low-altitude and magnetospheric spacecraft. *Journal of Geophysical Research: Space Physics*, *123*, 8390–8406. https://doi.org/10.1029/2018JA025867

Received 3 JUL 2018
Accepted 3 OCT 2018
Accepted article online 10 OCT 2018
Published online 27 OCT 2018

Abstract Motivated by ongoing discussion regarding the magnetic configuration in the near-Earth and midtail regions and its role in populating the inner magnetosphere during long-duration steady magnetospheric convection (SMC) events, we analyze a rich collection of observations during ~10 hr of strong, steady solar wind driving. Auroral boundaries and regions of stretched and dipolarized magnetic field in the plasma sheet were monitored using solar electron loss cone anisotropy observed by low-altitude spacecraft. Following a southward turning of the interplanetary magnetic field and a subsequent 3- to 4-hr period of large-scale substorm-related reconfigurations and plasma injections, the near-Earth magnetic configuration evolved into a nonstandard type, which lasted until the end of this SMC event (5 hr). During that time a dipolarized region with complicated Bz landscape persisted in the midtail, while the configuration was very stretched in the near tail. This was manifested as a highly depressed magnetic Bz component at geostationary orbit and as persistent nonadiabatic electron scattering at the periphery of the outer radiation belt. In addition, in situ observations suggest that a thin current sheet extended longitudinally toward the dawn terminator. In the return convection region near the terminator, observations of this azimuthal current sheet were sporadically interrupted/modulated by earthward convecting plasma structures, either remnants of reconnection-produced plasma bubbles or flapping waves. The hybrid magnetotail configuration (dipolar in the midtail and stretched in the near tail) observed during this long-duration SMC event poses a challenge for empirical magnetospheric modeling.

1. Introduction

Although the solar wind is rarely steady, relatively long (hours to days) time periods, when the solar wind driver (e.g., the southward interplanetary magnetic field [IMF] Bz component and the related solar wind Ey) continues to be strong, have sometimes been observed. Such periods generate strong magnetospheric convection accompanied by perturbations in various magnetosphere-ionosphere system parameters. Global dynamic magnetospheric reconfigurations, magnetospheric substorms (Akasofu, 1964), recur often during prolonged intervals of intense solar wind driving (Huang et al., 2003). Even though periods of nearly steady state global response to prolonged driving occur less frequently than substorms and are difficult to identify objectively, such periods, referred to as convection bays (Pytte et al., 1978; Sergeev et al., 2001), balanced reconnection intervals (DeJong et al., 2008, 2009), or steady magnetospheric convection (SMC) events (Sergeev, 1977; Sergeev et al., 1996), exist. Understanding the characteristics of such steady response to intense solar wind driving is important for two reasons: First, this is a fundamental response of the magnetospheric system to strong driving. Second, it is of significant practical interest because it may constitute an important subclass of magnetic storms, which are essential contributors to the space weather.

During an SMC event, the total magnetic merging rates are nearly balanced on the dayside magnetopause and on the X-type neutral line extending across the nightside magnetotail (DeJong et al., 2009; Milan et al., 2007). Observations confirm that the average magnetic flux transport in the plasma sheet matches these rates (Dmitrieva et al., 2004), indicating that the magnetotail operates in a nearly-continuous, *flow-through* convection regime. Unlike substorms, SMCs exhibit no significant energy loading and unloading. However, it is unclear how such a nearly continuous state of convection can be maintained in a *typical* magnetotail configuration deduced from long-term statistical averaging of satellite measurements, which has a monotonically decreasing northward magnetic field Bz component in the tail current sheet (CS). As widely discussed following the publication of the Erickson and Wolf (1980) paper, such a configuration is stable

against interchange-/ballooning-type perturbations, and it resists earthward convection in the midtail and near-Earth plasma sheet (this is often referred to as the *pressure crisis*). Hau et al. (1989) and Hau (1991) found two-dimensional tail-like equilibrium configurations with a nearly flat $pV^{5/3}(r)$ profile (this parameter is referred to as the plasma tube entropy, where V is the volume of a unit magnetic flux tube) in which a flow-through regime of adiabatic convection is possible between, roughly, the 12 R_E and 30–40 R_E regions. Such hybrid configurations include a local Bz minimum at geocentric distance ~12 R_E and a region of enhanced Bz farther down to the midtail. The length of the dipolarized midtail region may be 10 to 30 R_E. These two regions are separated by an extended region of tailward Bz gradient, where flow-through convection is possible. However, it is not clear to what extent such configurations are relevant in three dimensions, where a strong dipole-like magnetic field and increased thermal pressure in the near tail divert plasma azimuthally around it on either side of midnight. An observational test of the hypothesis that such a magnetotail configuration enables or facilitates continuous convection is important for understanding how the magnetotail averts the pressure crisis.

The first such evidence during prolonged SMC events was presented in Sergeev et al. (1994; and updated in the review by Sergeev et al., 1996). They summarized in situ observations supported by adaptive modeling and showed that the inner plasma sheet is thin and has a stretched magnetic field (as is common during the substorm growth phase), whereas the midtail plasma sheet is thick and displays an enhanced Bz (as is typical during the substorm recovery phase). Such a hybrid configuration resembles the steady adiabatic convection equilibrium solutions of Hau et al. (1989). However, the in situ observations analyzed by Sergeev et al. were made with a sparse coverage and were available in only a few events. Because of the very limited data used to constrain their models, their adaptive modeling results serve as an illustration rather than a proof of the expected hybrid configuration. Since then, observational and modeling investigations that included larger data sets and more comprehensive simulations have provided somewhat differing results.

Statistical surveys of SMC events using THEMIS and Geotail observations in the near and midtail regions have mostly confirmed the basic features of the aforementioned hybrid configuration. Kissinger et al. (2012) and Pulkkinen et al. (2013) found a very stretched configuration in the near tail (with an average Bz depression as large as ~60 nT around the nightside portion of geostationary orbit, see, e.g., Figure 4 of Pulkkinen et al., 2013). Kissinger et al. (2012) found an average Bz typical of the substorm recovery phase beyond 13 R_E, which implies that the transition region between inflated and dipolarized regions is somewhere between 9 and 12 R_E (see also Rong et al., 2014). According to these authors, however, during these SMC events, the high total pressure region extends to radial distances of ~15 R_E and causes fast earthward flows to be diverted toward the dawn or dusk flanks and then continue to the dayside. This flow pattern is distinctly different from those in 2-D models, also perhaps implying that the inner magnetosphere region is considerably screened from earthward convection. Whether this is true has yet to be demonstrated.

Moreover, Pulkkinen et al. (2013) concluded that during SMC events, the magnetic configuration in the inner region undergoes a systematic evolution from a more dipolar to a more stretched configuration, so SMC events were suggested to resemble an extended substorm growth phase. So can SMCs be described by the steady state models? In all the abovementioned statistical studies the SMC event identification was based solely on the AL and AU indices and their variability, and the events were limited to 90 min, which is smaller than the entire duration of a substorm. Walach and Milan (2015) criticized this approach, noting that the average duration of SMC events in those lists was only 3.2 hr, being not too different from the substorm time scale. As a result, one may rightfully question the validity of conclusions of those statistical SMC studies.

Stephens et al. (2013) used a new *nearest neighbors* approach to mine spacecraft data in analogous events for statistical modeling based on the TS07D model. Like Kissinger et al. (2012), they found strong plasma pressure buildup far beyond geosynchronous orbit. They also demonstrated very different tail Bz distributions during two long SMC time intervals, including those with a deep minimum of the equatorial magnetic field Bz near the transition region, as well as new states with a weak Bz minimum and a larger equatorial magnetic field confined to a relatively short tail region. However, time periods with similar Bz, Dst, and dDst/dt (parameters used in the *nearest neighbor* search) can also correspond to dynamical states other than SMC events, so again there is no guarantee that their modeling results refer exclusively to SMC configurations.

The most advanced simulation of an SMC event was reported by Yang et al. (2012). They ran a few different RCM-E simulations for an event that occurred on 13 March 2009 and compared their results with THEMIS and GOES observations. Their run D produced the best agreement with multipoint observations, including the magnetic field, plasma moments, flux transport, and cross-tail current densities at THEMIS in the near-Earth region, as well as the magnetic field at GOES-12 in the dusk sector. They concluded that during this SMC the plasma sheet was dipole-like and without any Bz minimum in the near-Earth plasma sheet. They argued that this configuration occurred because the flux tubes were depleted substantially of their plasma content at the outer boundary of the dipolarized plasma sheet (at the outer boundary of the simulation domain, $r \sim 22\ R_E$) over a wide local time sector. That event, however, was also brief (only 2 hr long), and during it the solar wind flow pressure doubled in magnitude, so the relevance of these results for prolonged SMC events is also questionable.

Therefore, a number of questions remain regarding—whether such a hybrid magnetotail configuration exists and how it varies during SMCs, as well as about the timescales required to identify an SMC event. In this paper we analyze an example of a prolonged SMC event during 10 hr of stable intense driving, paying close attention to the character and evolution of the magnetotail configuration. We use in situ observations in the inner magnetosphere (GOES and RBSP-A spacecraft) together with THEMIS observations in the return convection region of the plasma sheet, which provide important direct information about the magnetic field at several locations in the magnetotail. To assist in the large-scale survey of the tail configuration, we also apply a remote-sensing technique based on energetic electron observations from the low-altitude POES spacecraft and on DMSP particle boundaries. We also compare observations with predictions from a few models (including both empirical data-based models and global MHD simulation), to determine whether any of these models could reproduce a hybrid configuration during the SMC and help us to perform a magnetic mapping between the magnetosphere and ionosphere.

2. Event Description

2.1. General Description

The event of interest occurred on 19 May 2013, in response to prolonged, steady solar wind driving conditions, Figure 1a. After an active period and ~3 hr of quiescence (not shown), it started at about 0530 UT. According to OMNI data (from propagated ACE observations), a southward IMF turning was immediately followed by an increase in global magnetospheric convection as seen in the Polar Cap North (PCN) index.

The southward IMF turning and the subsequent IMF variations were also observed by Geotail in the near-Earth solar wind (at [14; −17; 7] R_E GSE) and by Cluster in the dawnside magnetosheath at [2; −17; −6] R_E (see their locations in Figure 1b). The solar wind was relatively slow (380–410 km/s) with density of 4–6 cm^{-3}. Before 08 UT the flow pressure was about 2 nPa and Cluster observed multiple bow shock crossings, after which the pressure decreased by a factor of 2 (~1 nPa) and Cluster finally entered the magnetosheath. Intense southward IMF and enhanced solar wind driving of the magnetosphere continued for ~10 hr. Between 09 and 15 UT small variations of both the solar wind and ground activity parameters occur (this time window is indicated by pink area in Figures 1 and 2). During this SMC event, the southward IMF was the largest component: it continued at approximately −5 nT (±0.5 nT) level until ~1520 UT, while Bx fluctuated around zero and By varied between 0 and +2 nT. The southward IMF episode was accompanied by intense convection (PCN index ~ 2–3 mV/m). The relatively weak variations in the enhanced auroral electrojets (Figure 2; AE up to 900 nT) explain the relatively weak Kp ~ 2. An enhanced ring current, manifested by a SymH decrease to −45 nT, almost reached the level of a moderate magnetic storm.

Figure 2 adds other important observations to characterize this event. The first is the Wp index, which gives the worldwide magnetic pulsation activity in the Pi2 range at midlatitudes (Nosé et al., 2012). This index shows a series of strong Pi2 bursts during the substorm commencing a strong driving interval (starting at 0629, 0659, and, the strongest, 0741 UT). It also shows a strong Pi2 burst at 1510 UT, just before the start of IMF variations in the concluding part of the SMC event. According to these observations, the interval between 09 and 15 UT is free of substorm activity, which is also consistent with GOES and RBSP spacecraft observations presented in the following section.

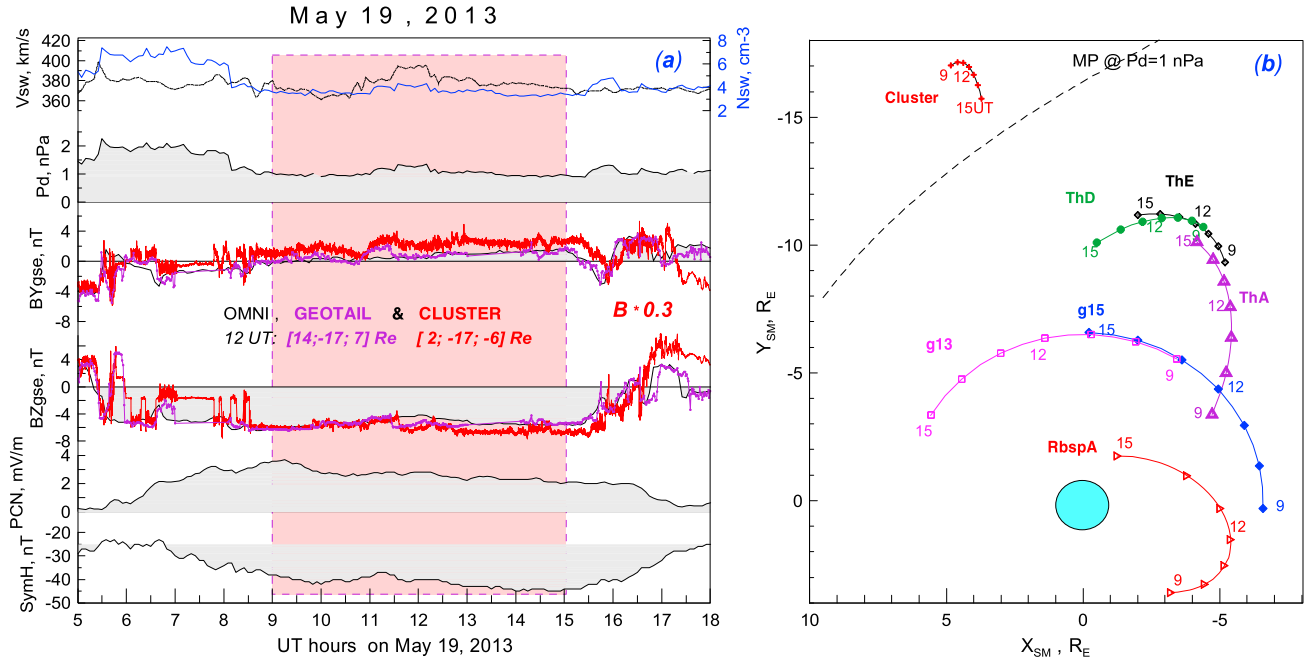

Figure 1. (a) Five-minute-averaged OMNI solar wind and ground activity data. (b). Trajectories of the magnetospheric spacecraft that contributed to our study between 09 and 15 hr UT. In Figure 1a, the Cluster magnetic field was scaled by a factor of 0.3 to compensate for interplanetary magnetic field compression in the magnetosheath.

The second important piece of information, regarding particle boundaries, came from Defense Meteorological Satellite Program (DMSP) satellite observations (the boundary nomenclature and identification procedures were described in Newell et al., 1996, and the data are available from http://sd-www.jhuapl.edu/Aurora/). From a number of routinely derived boundaries we selected the two that are most useful to characterize the magnetotail configuration and its changes. From them, the location of peak proton energy flux in the equatorward part of the auroral oval (b2i boundary) corresponds to the boundary between regions of adiabatic and nonadiabatic proton motion, known as the proton isotropy boundary (IB; see Newell et al., 1998). On the nightside, it is usually located in the inner magnetosphere just outside geostationary orbit. The locations of proton IB latitude on the nightside according to POES observations are also shown in Figure 2.

Another boundary (b5) was chosen to monitor the polar cap boundary (PCB), which is often used as a proxy of a topological boundary between open and closed magnetic field lines in the magnetotail. It is defined here as the most poleward of two similar boundaries derived from either electron or proton observations (b5e and b5i), each corresponding to an observed sharp drop in precipitated particle flux immediately before the highest-latitude region of very low auroral precipitation, identified as the polar cap, was observed. To better characterize the size of the polar cap, which is proportional to the total amount of open magnetic flux, as well as the size of equatorial oval from observations made at different local times, we show both quantities (b5 and b2i) in a special coordinate system. This coordinate system is based on the fact that both the PCB (according to Holzworth and Meng, 1975) and the brightest portion of the auroral oval during various conditions (Milan et al., 2009) are well fitted by circles with centers displaced statistically by 5° toward midnight from the corrected geomagnetic pole. Accordingly, to characterize the polar cap and auroral oval dimensions and their changes, at the top of Figure 2 we show the colatitudes of b2i and b5 boundaries in a coordinate system with a pole that corresponds to the center of the abovementioned statistical auroral oval.

The DMSP observations demonstrate equatorward expansion of the initially narrow auroral oval during the substorm growth phase (before 0630 UT) and significant poleward expansion of the oval during the subsequent expansion phase (especially after 0740 UT). The expanded oval seems to exist until 09–10 UT. At such high latitudes the PCB reappears again after 15–16 UT, at the end of the event. Because of the dipole diurnal rotation, after 09 UT the available DMSP orbits mostly crossed the dusk and dawn portions of the oval.

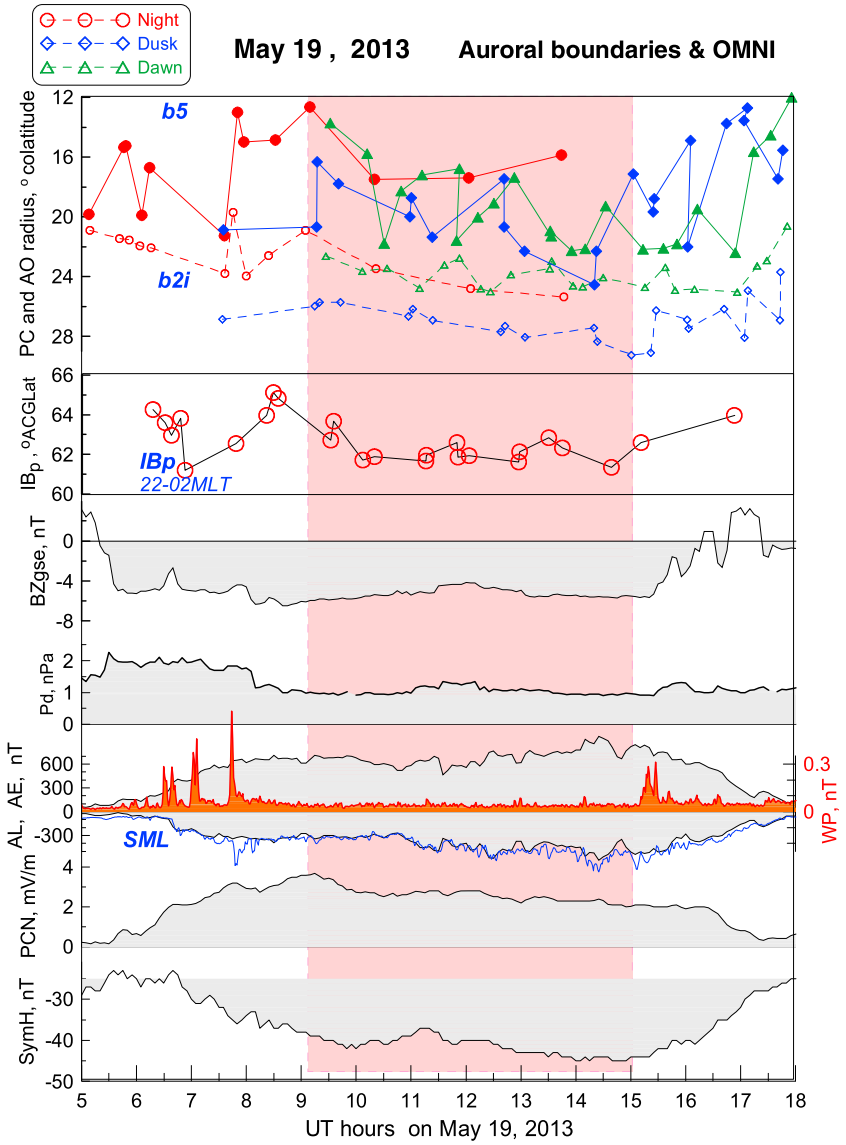

Figure 2. From top to the bottom: Time variations of DMSP auroral precipitation boundaries that characterize the polar cap boundary (b5, symbols connected by solid lines) and a proxy of proton isotropy boundary (b2i, connected by dashed lines); proton isotropy boundary according to POES observations near midnight; solar wind dynamic pressure and interplanetary magnetic field Bz; AL and AE indexes with superposed pulsation activity index WP (red); magnetic activity indices Polar Cap North (PCN), and SymH. DMSP boundaries are color coded for different sectors, including dusk (16–21 hr magnetic local time [MLT], blue), night (21–03 hr MLT, red), and dawn (03–07 hr MLT, green). Their colatitudes are given in coordinates with the pole centered on the center of the statistical auroral oval (see text for details).

During a nonsubstorm time between 10 and 15 UT, the equatorward b2i boundaries gradually expand by ~2° latitude. This expansion may be associated with the gradual ~5 nT SymH decrease observed during this time. Duskside b2i latitudes are ~3° lower than those measured on the dawnside, indicating that the duskside inner magnetosphere is more inflated than its dawnside counterpart, which may indicates an effect of the partial ring current. No comparable equatorward shift of proton IB is observed by POES on the nightside. There could also be a tendency for a comparable increase of the PCB dawn-dusk size, but the b5 boundary at this time shows large variations superimposed on this trend. An inspection of far ultraviolet DMSP auroral observations (not shown here) reveals that those variations reflect complicated dynamical variations of structured and localized intense auroras developing near the PCB rather than any large-scale dynamical changes in the polar cap.

The OMNI solar wind parameters have been confirmed to represent actual parameters in the near-Earth solar wind (Figure 1a). We used them to run several magnetospheric models, including a recent TA15 statistical prognostic model (Tsyganenko & Andreeva, 2015) and TS05 and TS07D models (Tsyganenko & Sitnov, 2005, 2007). These models differ in the size and distribution of spacecraft measurements used to construct them as well as in the functions used to describe current systems and their dependence on the solar wind parameters. The applied version of TS07D (courtesy of M. Sitnov and G.Stephens) used the data-mining algorithm described in Sitnov et al. (2008) and its substorm modifications (Stephens et al., 2017) with the following parameters: number of basis function expansions in azimuthal angle $M = 6$, number of radial functions $N = 8$, and number of field-aligned current modules NF = 16; the size of the data-mining bin was L_{NN} = 16,000 points in this case. We also used the Community Coordinated Modeling Center facility (https://ccmc.gsfc.nasa.gov/) to run the LFM version of a global MHD model between 04 and 18 hr UT on 19 May 2013 (run # Victor_Sergeev_042717_1).

2.2. In Situ Observations in the Inner Magnetosphere

Figure 3 provides a survey plot of magnetic field and energetic electron observations by two geosynchronous spacecraft (GOES-13 and GOES-15) spanning the nearmidnight-to-dawn sector of the inner magnetosphere (see Figure 1b). Between 0630 and 0830 UT both spacecraft registered energetic particle injections accompanied by Bz increases (local dipolarizations) that correspond well to three intense Pi2 pulsation bursts shown in Figure 2. Soon after having relaxed from substorm injections, the energetic electron flux continued to decrease (especially at the highest energies, suggesting adiabatic changes) in association with the Bz-component decrease at GOES-15, down to −30 nT below the TA15 prediction (purple line in Figure 3). At this time the By component also increased, up to 20–30 nT above the TA15 prediction. As they were observed during the time period of interest, between 09 and 15 UT, these changes demonstrate very strong magnetic field stretching in the postmidnight-dawn local time sector, significantly stronger than that predicted by the TA15 model for the given solar wind conditions. The character of energetic electron variations also changed at this time. Unlike the bay-like, energy-dispersed variations between 0630 and 0830 UT, which are typical of substorm injections, short-scale flux increases without any evident dispersion were sporadically observed in low-energy channels. Because of the stretched magnetic field, they map to more distant regions in the magnetic equatorial plane. They may be closely related to the short-duration sporadic activity observed by THEMIS spacecraft in that local time sector, which will be considered in the next subsection.

During the time period of interest, the RBSP-A spacecraft traversed the inner magnetosphere near its apogee in the premidnight local time sector (Figure 1b). It observed a strong depression of the Bz component consistent with GOES observations, this component was below that predicted by the TA15 model by 20–40 nT (see Figure S1 in the supporting information). Also, Figures 3 and S1 consistently show that the global MHD simulation produced an inner magnetospheric configuration significantly less stretched than observed and than predicted by the TA15 model.

2.3. THEMIS Observations

During the event of interest, the three THEMIS spacecraft probed the postmidnight-dawn portion of the plasma sheet, providing spin resolution plasma observations only in reduced mode. The ThE spacecraft followed the ThD spacecraft along nearly the same trajectory; after 10 UT they were at 11–12 R_E near their apogees. At 12 UT, their geocentric solar magnetospheric coordinates were [−2.6; −11.1; 1.2] at ThD and [−3.8; −10.8; 1.6] at ThE. As shown in Figure 4, at that location, slightly above the magnetic equator, they observed a spectacular increase of highly fluctuating By component after 09 UT. After 12 UT it reached peak values up to 40–50 nT, well above the values predicted by any model. The Bz component was also fluctuating, but its variations were smaller. Because By is a nearly radial component at this location (Bx was smaller, see, e.g., Figure 5) and because simultaneous By growth was observed also in the postmidnight-dawn sector of the geostationary orbit (Figure 3), the large By may indicate a formation of an intense azimuthal CS. There was no indication of such CS growth before 09 UT.

The ThA spacecraft followed ThD and ThE along a similar orbit, but with a 4- to 5-hr lag. It crossed the inner region outbound before reaching 9 R_E distance at 1145 UT. Here ThA data confirmed the GOES observations of significantly depressed Bz component in the inner magnetosphere (up to 20–30 nT below the TA15 model prediction; Figure 4, bottom). Soon after 10 UT ThA also observed strong growth of a fluctuating By

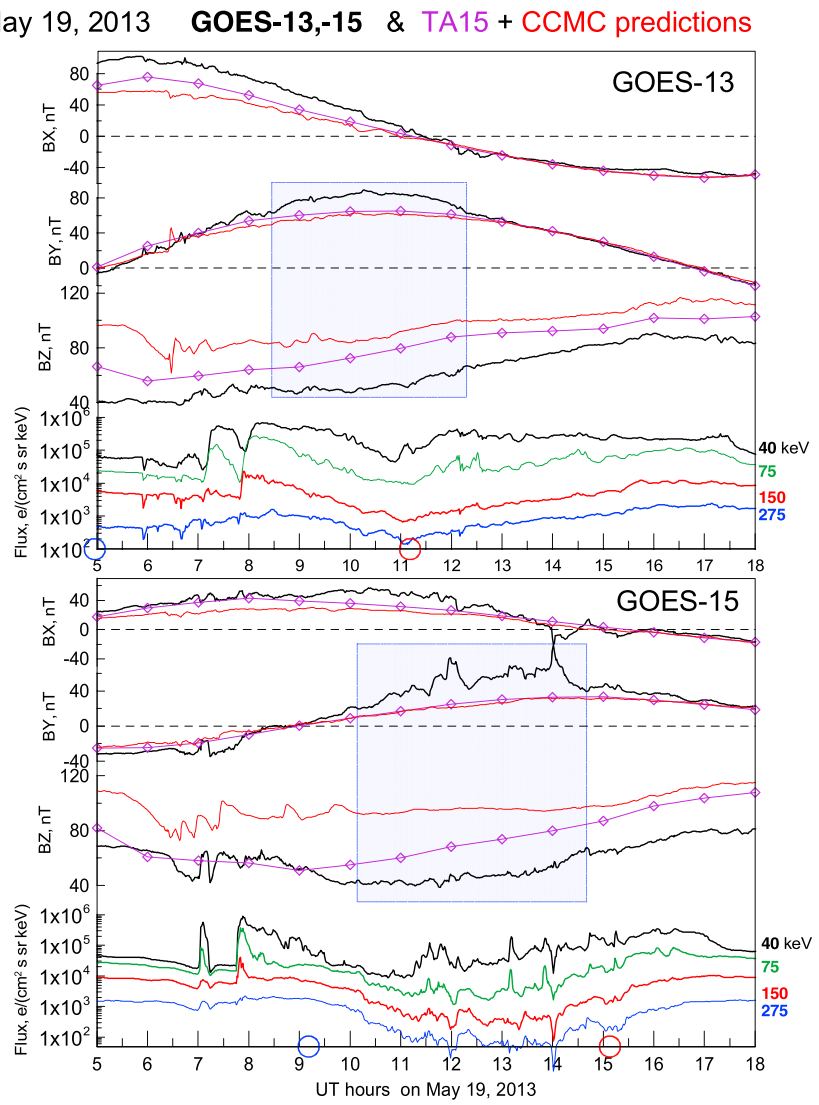

Figure 3. Observations at geosynchronous satellites GOES-13 and GOES-15, including Cartesian magnetic field components in the SM coordinate system and energetic electron fluxes from the EPS-MAGED telescope. Magnetic field predicted by the recent magnetospheric model TA15 and by global LFM simulation is shown for reference. Magnetic midnight (blue) and dawn (red) are indicated by circles at the bottom of each plot. The shaded area indicates regions of most tailward stretched magnetic field orientation as observed by GOES-13 and GOES-15.

component, up to 50 nT above the TA15 predictions. Taken together, the data of GOES-15 and all three THEMIS spacecraft confirmed the presence of a thin azimuthal CS during the second stage of the SMC event, between 10 and 15 UT.

The fluctuating behavior of this atypical CS appears puzzling. Although requires a special thorough study, in Figure 5 we present a fragment of observations that suggests a simple explanation. This fragment documents a sequence of magnetic field and plasma parameter variations observed at ThD and ThE, which all look surprisingly similar at both spacecraft when shifted in time by 3.6 min, as it was done in Figure 5. Such a shift implies sunward propagation of plasma structures from ThE to ThD (separated mainly in X by ~1.3 R_E) with a velocity of ~40 km/s, which is consistent with the measured average proton bulk flow. A plausible interpretation of this fluctuating By appearance is that the azimuthal CS signatures are modulated by localized sunward convected structures, possibly either the remnants of BBFs produced by time-varying reconnection, or the flapping wave (flapping waves were also observed in the dawnside plasma sheet; Yushkov et al., 2016). We recall that these observations were made in the region of return convection near the dawn terminator

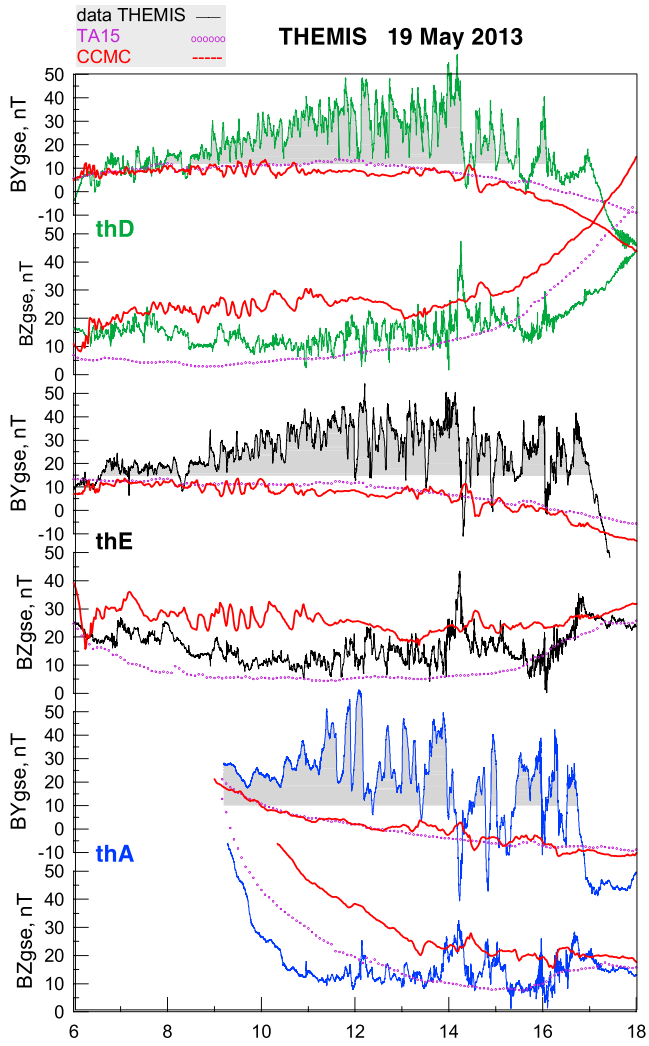

Figure 4. Magnetic observations at three THEMIS spacecraft in the dawnside plasma sheet together with reference magnetic fields predicted by TA15 and global MHD model. Strong fluctuated By component, which grew between 09 and 12 UT and continued until the end of the steady magnetospheric convection, is emphasized by gray shading.

at 10 to 12 R_E. More detailed investigation of these interesting structures requires special study in a future paper.

3. Low-Altitude Observations

Remote sensing of nonmonotonic radial distributions of the equatorial magnetic field from low-altitude observations of energetic electron precipitation has been recently discussed in application to the growth phase configuration (Sergeev et al., 2018) so we only briefly repeat the basics of this method referring the reader to this paper for some details.

During each crossing of an energetic charged particle through the CS, it undergoes a nonadiabatic pitch angle (PA) change, the amplitude of which depends on the ratio of the magnetic field curvature radius (Rc) to the particle gyroradius (ρ). The value of this ratio depends on the equatorial magnetic field and particle characteristics as

$$Rc/\rho \approx Bz^2/(G\, dBr/dz) = Bz^2/(G\, \mu_0\, j) \quad (1)$$

The particle rigidity parameter $G = mV/e$ combines the particle mass, velocity, and electric charge. From previous trajectory simulations (Delcourt et al., 1996; Sergeev & Tsyganenko, 1982) we know that for very small PAs, the PA scattering amplitude becomes comparable to (or exceeds) the loss cone (LC) width if $Rc/\rho \leq 8$ at the CS center in standard CS models. This field line curvature (FLC)-related PA scattering mechanism is responsible for many important magnetospheric phenomena. As $Rc/\rho < 8$ for protons in the vast area of the equatorial plasma sheet, the strong scattering provides isotropic proton distributions in the plasma sheet and related isotropic proton precipitation into the ionosphere, which forms the proton auroral oval. The low-latitude border of this isotropic precipitation, the IB, corresponds to the b2i boundary plotted in Figure 2. The proton IB field line in the magnetosphere stays in the outer part of the dipole-like region where the magnetic field is about 30–60 nT (depending on the concurrent current density j); the IB latitude strongly correlates with the magnetic field in the conjugate sector of geostationary orbit (e.g., Donovan et al., 2003; Newell et al., 1998; Sergeev et al., 1993).

As electrons have a much smaller gyroradius than protons, their FLC scatter becomes effective at greater distances from the Earth in the plasma sheet. For energies 30–100 keV this scatter occurs in CS regions where Bz is smaller than 5–10 nT (see, e.g., computations for typical CS conditions in Figure 1 of Sergeev et al., 2018). Such a Bz threshold is suitable to differentiate observationally between regions of CS with small Bz ($<$5 nT) and those with dipolarized CS configurations, including bursty bulk flows (BBFs), where Bz $>$ 10 nT. Accordingly, CS or dipolarized regions can be identified by low-altitude spacecraft observations of either isotropic precipitation of energetic electrons or their anisotropic LC distributions, respectively.

Here we use observations from polar-orbiting low-altitude POES-type satellites. Each of the six currently available satellites carries identical detectors to measure the energy fluxes of protons and electrons between 0.05 and 20 keV as well as of more energetic particles. In particular, they measure the integral electron fluxes at nominal $>$30, $>$100, and $>$300 keV energies nearly simultaneously inside and outside the LC (Evans & Greer, 2000). The ratio of precipitated to trapped particles (I_0/I_{90}) provides a diagnostic of the LC filling rate. A specific limitation of this sensing method is that the energetic electron fluxes may be low in some portions of the tail plasma sheet, resulting in large uncertainties in the precipitated-to-trapped flux ratio estimates in these regions. Fortunately, during the major electron-rich solar particle event in May 2013 (including May 19), an intense flux of tracer electrons was always available, with a count rate of $>$30 keV solar electrons in the polar cap and plasma sheet exceeding 50 counts per second (Sergeev et al., 2018).

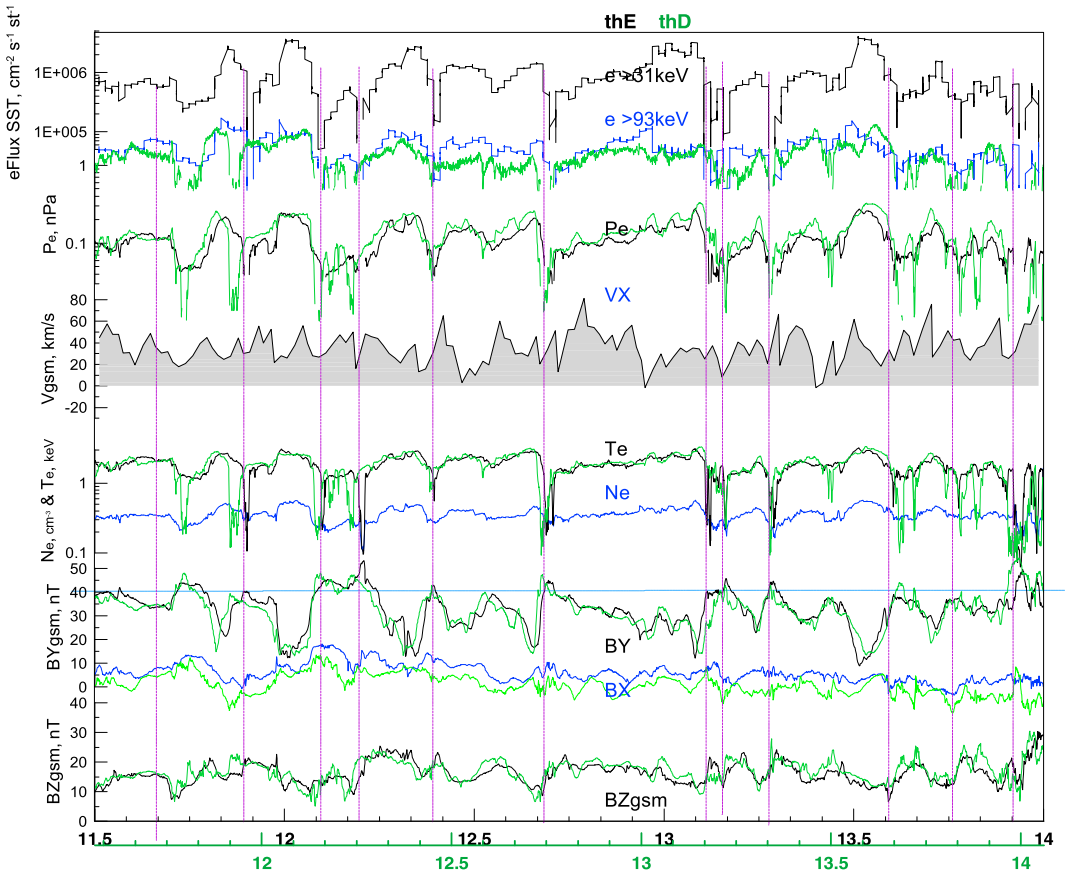

Figure 5. Details of observations at two THEMIS spacecraft. ThE (black/blue lines) follows ThD (green lines) with a separation of ~1.5 R_E along the trajectory (Figure 1b). Note that time axis at ThD (green axis) is shifted by 3.6 min to the earlier time against thE (black axis) to emphasize sunward propagation of a minute-scale plasma structures.

Figure 6 shows two examples of NOAA-19 observations during its traversals of the southern auroral zone along the ~02 hr magnetic local time (MLT) meridian, which occurred during our SMC event. In both cases upon having entered into the polar cap on the high-latitude side of the auroral zone, the spacecraft detected a stable homogeneous isotropic precipitation of solar energetic electrons. Moving back toward the lower latitudes in the auroral oval (along the expected direction of plasma convection in the tail), we see steadily increasing fluxes of energetic electrons in the plasma sheet, which indicate that the acceleration process is in progress. The 1.5–2° AACGLat wide most poleward part of the oval contains isotropic precipitation ($I_0/I_{90} = 1$), suggesting that it comes from a CS area with a small Bz value. This may be a CS portion adjacent to the active reconnection line, where the largest peaks of auroral electron energy flux have also been detected. Further equatorward, electron fluxes are always high, but LC fluxes decrease considerably. This means that the FLC scattering is not operating anymore and suggests that here the spacecraft was in the dipolarized plasma sheet region (marked as DIP in Figure 6). The conjecture of the FLC scattering precipitation mechanism is furthermore supported by noticing that the I_0/I_{90} ratio is systematically higher for 100 keV electrons than for 30 keV electrons (blue curve on the bottom plot lies above the black one), as expected for this mechanism. Finally, on the low-latitude side the spacecraft encounters the outer radiation belt with high but strongly anisotropic energetic particle fluxes. The radiation belt boundary (oRB in Figure 6) is defined here as the point where the particle flux in the 100 keV e-channel increases sharply above its plasma sheet level.

In addition to many similarities, there are clear differences between two spacecraft passes in the low-latitude region, near the radiation belt boundary. Although we see localized regions of nearly isotropic electron precipitation in the $E > 30$ keV channel, electron precipitation in the $E > 100$ keV channel behaves differently. In case (a) the I_0/I_{90} ratio for high-energy precipitation is comparatively small, indicating that FLC scattering is not operating there. Such 30 keV precipitation spikes in the radiation belt region are normally produced

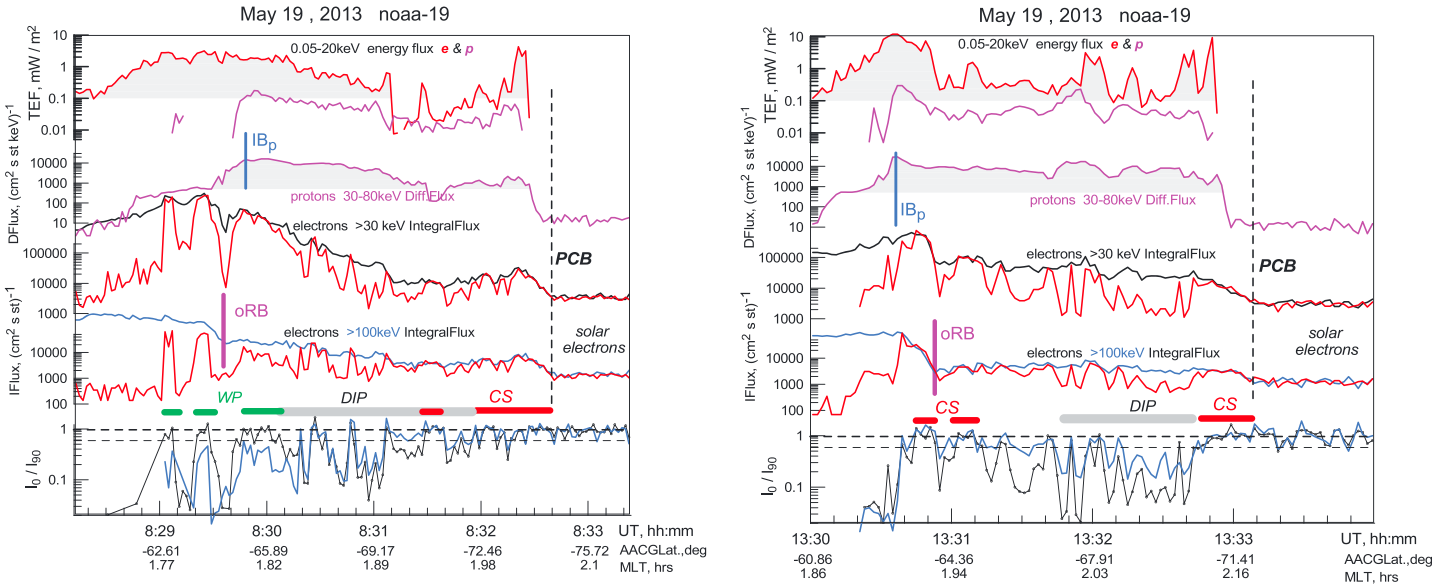

Figure 6. NOAA-19 observations during two passages (a and b) across the postmidnight auroral zone. From top to bottom: Energy flux of 0.05–20 keV electrons and protons; differential flux of 30–80 keV protons, which characterize the plasma sheet pressure distribution; integral fluxes of >30 and >100 keV electrons, including both precipitated (red trace) and trapped particles (black trace); ratio of precipitated to trapped fluxes of $E > 30$ keV (black) and $E > 100$ keV (blue) electrons. Also shown are the proton isotropy boundary (IBp, blue), the outer boundary of the radiation belt (oRB, purple), and the polar cap boundary (PCB, dashed black line). Schematic of the region identification is shown on the bottom, including the current sheet (CS, red), dipolarized plasma sheet (DIP, gray), and wave-induced precipitation bursts (WP, green) regions.

by wave-particle (usually whistler wave) interaction (denoted as WP in Figure 6a). In striking contrast, in case (b), $E > 100$ keV electrons are virtually isotropic in the extended region between −63° and −67° including 30 keV precipitation spikes, and the I_0/I_{90} ratio is always higher than that in the $E > 30$ keV channel. Such a feature, the intense isotropic precipitation spike on the low-latitude side of the oRB is rather common in POES observations, and previous investigations have provided strong evidence of its formation by the FLC scattering process (see, e.g., Sergeev et al., 1996, 2012).

Having introduced the regional identification procedure, we present meridional distributions of the LC filling rates of >30 and >100 keV electrons, along with the trapped flux of $E > 100$ keV electrons in Figure 7. This survey of subsequent NOAA-19 passes, all of which traversed the same postmidnight MLT sector, helps characterize the evolution of the plasma sheet magnetic configuration in the course of the SMC event. The first pass (a) occurred just before the start of the event. Here the isotropic precipitation of solar electrons in the entire plasma sheet (emphasized by shading in Figure 7) indicates that Bz values are small everywhere in the plasma sheet and that no additional electron acceleration occurs there. During the substorms (passes b and c), the I_0/I_{90} ratio dropped significantly indicating a dipolarized magnetic field in the plasma sheet. This occurred with a generally enhanced energetic particle flux, indicating a concurrent electron acceleration in the plasma sheet. An exception here is a region of incessant isotropic precipitation near the outer PS boundary (contiguous to the expected reconnection line), a general feature of all POES passes. Precipitation bursts of >30 keV electrons (with much lower PA scatter at energies >100 keV, typical of wave-induced precipitation) are seen inside the radiation belt region during substorm injections (passes b and c). In the dipolarized part of the plasma sheet the electron LC filling rate changes irregularly, indicating a complex Bz structure. This irregular dipolarized magnetic configuration in the middle part of the plasma sheet was observed throughout the entire SMC event. Starting at ~10 UT (passes e through j) a distinct isotropic precipitation region also appears near the outer boundary of the radiation belt (this region is later referred to as the inner CS).

To investigate the geometry and stability of the inner CS, we surveyed all POES crossings of the near-midnight region (between 21 and 03 hr MLT) that occurred between 10 and 15 UT. The traversals and the region identification (see legend) are shown in Figure 8. To simplify the presentation, the CS regions were identified as those with $I_0/I_{90} \sim 1$ at least during three subsequent observation points (at 2-s resolution of

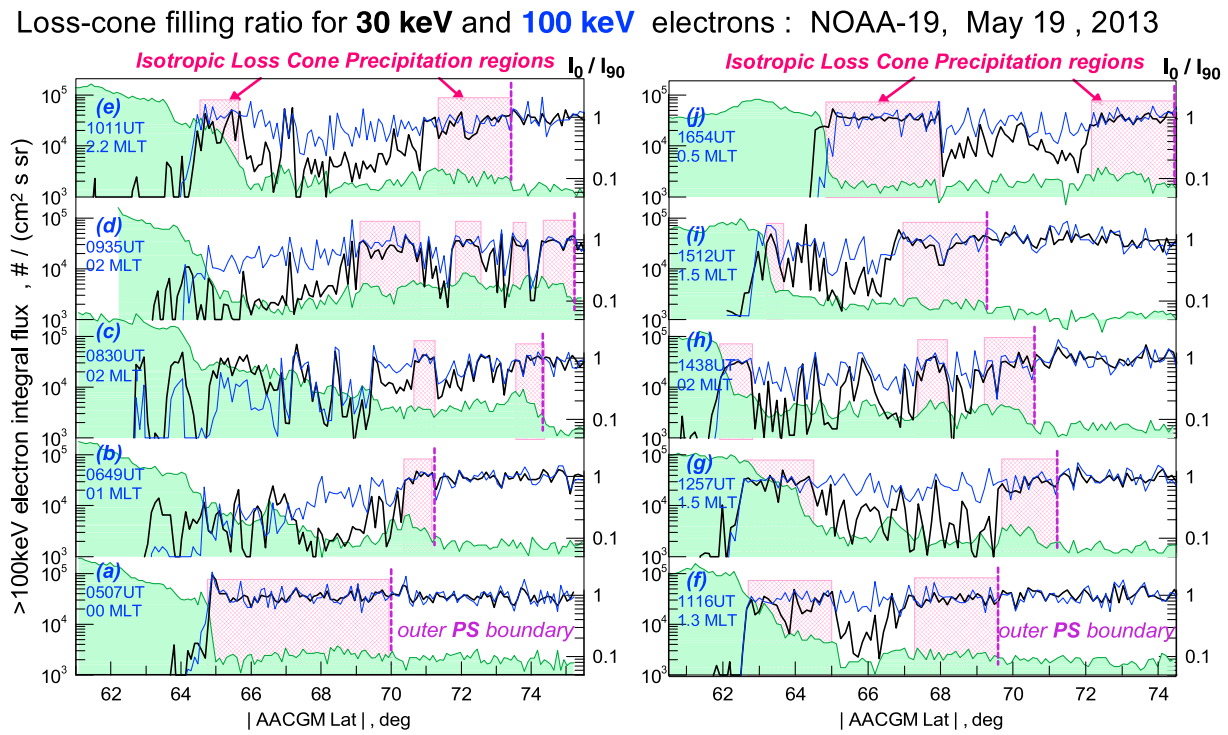

Figure 7. Selected examples of NOAA-19 observations covering the entire duration of a steady solar wind driving event. Each panel includes the loss cone filling ratio (I_0/I_{90}, vertical axis on the right) of 30 and 100 keV electrons (in black and blue as in Figure 7) together with trapped fluxes of >100 keV electrons (green line, shaded area). The outer plasma sheet (polar cap) boundary is shown by the vertical line; the red shading helps to show the extended isotropic precipitation regions (with more than three subsequent measurements with I_0/I_{90} ~ 1).

POES data). Similarly, gaps with fewer than three points inside extended CS regions were ignored. With such filtering, the pattern observed by each of four POES spacecraft (Metop-1 and Metop-2, NOAA-16 and NOAA-19) recurred very systematically from one pass to the next one. This pattern included the outer CS region near the PCB and the inner (near-Earth) sheet, separated by an extended dipolarized region. The inner sheet remained ~1–2° poleward of the proton IB and its width varied between 0.5 and 2° of latitude; that CS usually included the outer radiation belt boundary.

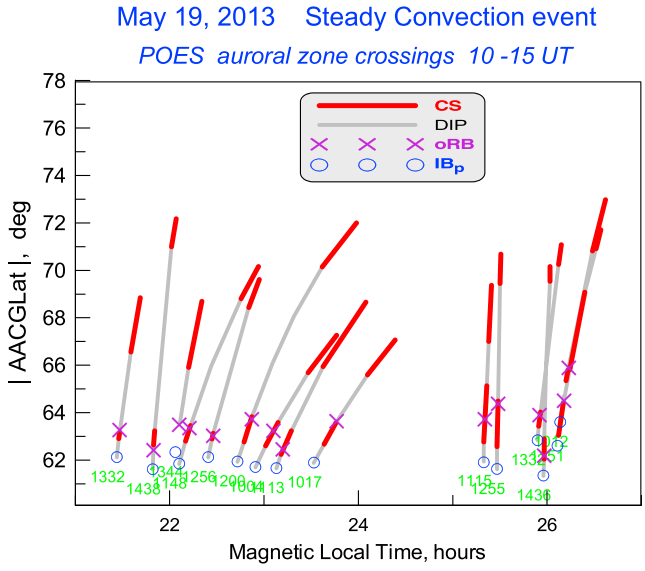

Figure 8. Summary of POES spacecraft traversals of the auroral region between 21 and 03 hr MLT that occurred between 10 and 15 hr UT. Current sheet and dipolarized regions as well as proton isotropy boundaries and outer radiation belt boundaries are also shown. The highest points on every trace correspond to the polar cap boundary.

4. Discussion

4.1. Magnetotail Structure During Steady Convection Event

The event we analyzed is a good example of a steady convection event. Solar wind driving, which was strong (IEF ~2 mV/m, IMF Bz ~ −5 nT) and steady, continued for ~10 hr with small variations, especially during the last 6 hr (between 09 and 15 UT). The concurrent solar wind and IMF OMNI data are reliable, as confirmed by two near-Earth monitors, Geotail and Cluster. During that time period, the traditional indices (PC, AU/AL, and SymH) indicated enhanced convection, and the auroral electrojet and ring current activity reached a level typical of moderate storms. Despite the rather variable b5 boundary, the PCB colatitude was on average about 16–22° between 10 and 15 UT, which corresponds to a 0.7–1 GWb polar cap magnetic flux, typical of SMC events (DeJong et al., 2009; Hubert et al., 2017). The short-term variability of the auroral indices was low, making the event consistent with an AL-based SMC identification procedure recently used by Kissinger et al. (2010). During the first 3–4 hr after the start of intense driving, signatures of substorm development,

including expansion and then contraction of the PCB (b5 in Figures 2 and 7), multiple Pi2 onsets, and particle injections to the geostationary orbit (Figures 2 and 3), were observed. Also, the plasma sheet displayed a dipolarized configuration accompanied by energetic particle acceleration (Figure 7). After ~09 UT, while the solar wind driving still continued to be intense and steady (Figures 1 and 2), the near-Earth configuration changed and remained in this new state for 5–6 more hours until the end of the event. The key observations during this stage of the SMC event are consistent with a number of previous findings. In a qualitative sense, our observations confirm the continuous 5-hr presence of a hybrid configuration, a dipolarized magnetic field in the midtail plasma sheet (presumably between 12 and 30 R_E) coexisting with a stretched configuration in the near tail, as first shown by Sergeev et al. (1994, 1996) and later confirmed by Kissinger et al. (2012) and Pulkkinen et al. (2013).

In POES observations (Figures 6 and 7) the dipolarized plasma sheet is observed as a region with depressed LC energetic electron fluxes, often combined with enhanced trapped fluxes that indicate ongoing particle acceleration. In this region, the LC flux ratio is $\ll 1$ and highly variable, indicating strong spatio-temporal variability of the Bz^2/j parameter in the plasma sheet that controls the LC filling process. This variability can be related to fast flow structures (BBFs), which are more frequent in the midtail during SMCs (Kissinger et al., 2012; Pulkkinen et al., 2013) and contribute to the variable Bz landscape in the plasma sheet. An important result of Kissinger et al. (2012) is that the total pressure is significantly enhanced at distances up to $r > 15$ R_E, which explains the deflection of average flows toward the flanks in this part of the tail. The enhanced pressure is consistent with the enhanced proton flux (both the total precipitated flux and the flux of >30 keV protons) observed in the dipolarized (empty LC) portion of the plasma sheet, at latitudes higher than the outer boundary of the radiation belt (see Figure 6).

The second element of the hybrid configuration is a stretched magnetic field in the inner magnetotail. In GOES observations it manifests as a significant Bz depression to ~30 nT below that predicted by the TA15 model and roughly 50 nT below the dipole values. Such depression values at GEO are consistent with those shown for the SMC events in the Pulkkinen et al. (2013) statistical study (see their Figure 4). Kissinger et al. (2012) reported that in "average SMC" event "Bz matches substorm growth phase values within 8 R_E and matches substorm recovery phase values outside of 13 R_E," which implies that the transition region between the inflated and dipolarized regions lies somewhere between 9 and 12 R_E. That rough estimate is consistent with our observation presented in Figure 4 (bottom), which shows that the relative Bz depression became substantially relaxed between 11 and 13 UT, when ThA moved outward from $r \sim 8.4$ to 10 R_E. An increase in the radial magnetic component accompanying the Bz depression at GOES-15, together with its simultaneous increase at ~11 R_E near the dawn terminator observed by the three THEMIS spacecraft, indicates the intensification (and/or thinning) of the CS. We have in situ observations only in the postmidnight-dawn MLT sector, where this enhanced electric current is directed azimuthally (toward the nightside).

The low-altitude observations provide important new information about development of the CS and the related Bz depression in the inner tail. The dipolarization (increased Bz and decreased current density j) raises the parameter Bz^2/j above the threshold for FLC scattering (section 4), and therefore, it is observed as highly anisotropic LC distributions of energetic electrons, as discussed above. Conversely, an intensification of the inner CS and/or Bz depression is manifested as isotropic electron precipitation near the outer boundary of the radiation belt, between the dipolarized part of the plasma sheet and the dipolar-like field in the inner magnetosphere. Such isotropic electron precipitation is known to occur there under different activity scenarios, it has been relatively well studied in previous works (see, e.g., Sergeev et al., 2012, for a brief summary and comparison with FLC predictions using data-adaptive magnetospheric models). In that region, the parameter Bz^2/j falls below the FLC scattering threshold level because either a local Bz minimum or a local j maximum has been formed. According to both data analyses (Artemyev et al., 2016) and global MHD simulations (Gordeev et al., 2017), Bz and j are inversely related in this part of the near-Earth tail during smooth tail reconfigurations. In view of this we will not distinguish below between these two possibilities and, for the sake of brevity, will refer to this region as the near-Earth Bz drop region. The latitudinal width of this inner isotropic precipitation region of ~1–2° (Figure 8) implies that its corresponding radial extent in the plasma sheet is about 3–5 R_E, based on a mapping equation from Sergeev et al. (2018) with Bz = 5 nT.

A stable component of the energetic electron precipitation pattern is the most poleward region of the isotropic electron precipitation from the plasma sheet, which is contiguous to the PCB and has a latitudinal scale of

1–2°—see examples in Figure 6 and overall summary in Figure 8. In previous studies this region was not considered to be a part of the hybrid SMC configuration. That region should correspond to a thin sheet-like reconnection outflow region contiguous to the active neutral line. The ongoing reconnection has a number of manifestations in the POES data. The first is an ~1° equatorward shift of the poleward boundary of keV electron and proton precipitation from the latitude where the energetic electron flux starts to rise above its solar electron flux level. The latter boundary (dashed vertical line in Figure 6) most closely represents the true boundary between the open and closed magnetic field lines, the reconnection separatrix. The latitudinal shift is caused by convective transport across the separatrix known as the velocity filter effect (e.g., Varsani et al., 2017; Zelenyi et al., 1990), which is a signature of an active reconnection process. The second manifestation, a smoothly increasing energetic electron flux, reflects a gradual energization of energetic electrons during their subsequent CS crossings in the presence of dawn-to-dusk electric field (Hoshino et al., 2001). The third manifestation of the ongoing reconnection is a strong peak of the auroral electron precipitated energy flux at the poleward oval boundary, which also indicates an active energization process. A poleward isotropic electron precipitation region is seen very frequently during both the substorm expansion phase (Figure 6a; see also Varsani et al., 2017) and the SMC steady phase (Figure 6b). The isotropic electron precipitation region represents the nightside reconnection region, the main generator of magnetospheric plasma sheet convection. The reconnection process is probably highly transient and localized as manifested, for example, by the complicated and variable Bz landscape in the dipolarized portion of the plasma sheet. The transience and localization of reconnection is probably related to the highly variable structure of the return convection region, directly observed near the dawn terminator by the THEMIS spacecraft (Figure 5). This also explains a multitude of localized transient activations observed in the plasma sheet and the auroral zone during long-lasting SMC events (Sergeev et al., 1996; Yahnin et al., 1994).

4.2. SMC Identification Aspects

During the substorm stage of our event, FLC-related isotropic electron precipitation near the radiation belt outer boundary was not observed by the POES spacecraft until ~09 UT. After that time it was registered on every POES traversal of the nightside oval (see Figures 7 and 8). This change in electron precipitation occurred simultaneously with magnetic field radial stretching at GOES-15 (Figure 3) and with growth of the radial B-field component at three THEMIS spacecraft (Figure 4). Taken together, this provides a clear indication that after the substorm subsided, the global magnetospheric configuration evolved into a hybrid configuration, in which it remained for 5–6 more hours.

This observation is important in the context of an intrinsic time scales of SMC state. A criterion of relatively long-duration, at least 3–4 hr (Sergeev et al., 1996), was previously applied to identify the SMC events. It was based on the argument that for an event exceeding the substorm growth phase time scale (about 1 hr) by a factor of 3–4, the large-scale inductive electric field in the plasma sheet is expected to be much weaker than that for the growth phase. In that case, large-scale time variations should not significantly affect the plasma sheet flow and equilibrium.

Recently, a procedure to identify the SMC events, based solely on the AL and AU indices and their variability (e.g., Kissinger et al., 2012; Pulkkinen et al., 2013), has been widely used. It has been highly popular because of its simplicity and the wide availability of the AE indices, which made it possible to generate long lists of events. To further increase the number of events, the lower limit on the duration of candidate events was relaxed to 90 min; as a result, the average duration of selected events decreased down to ~3 hr. These decreases might affect some conclusions of past SMC studies. For example, based on a statistical study, Pulkkinen et al. (2013) concluded that during SMC events, the field configuration undergoes systematic evolution from a more dipolar toward a more stretched configuration, and the SMC could be considered as a type of extended substorm growth phase. This conclusion is not fully confirmed in our study. The proton IB shifts only slightly in latitude on the nightside between 10 and 15 UT (Figure 8), and a weak trend of b2i expansion (roughly, ~2° decrease in 5 hr; see Figure 2) in the dusk and dawn sectors is observed, possibly related to a slight decrease in the SymH index. However, these changes are weak compared to those reported by Pulkkinen et al., and no strong substorm occurred after them in our case. Also, there were no comparable expansion of proton IB near midnight according to POES observations (Figure 2). We suggest that because of having included many short ($\lesssim$3 hr) SMCs, which most likely captured both substorm and relaxation stages, their results may not properly characterize the true steady

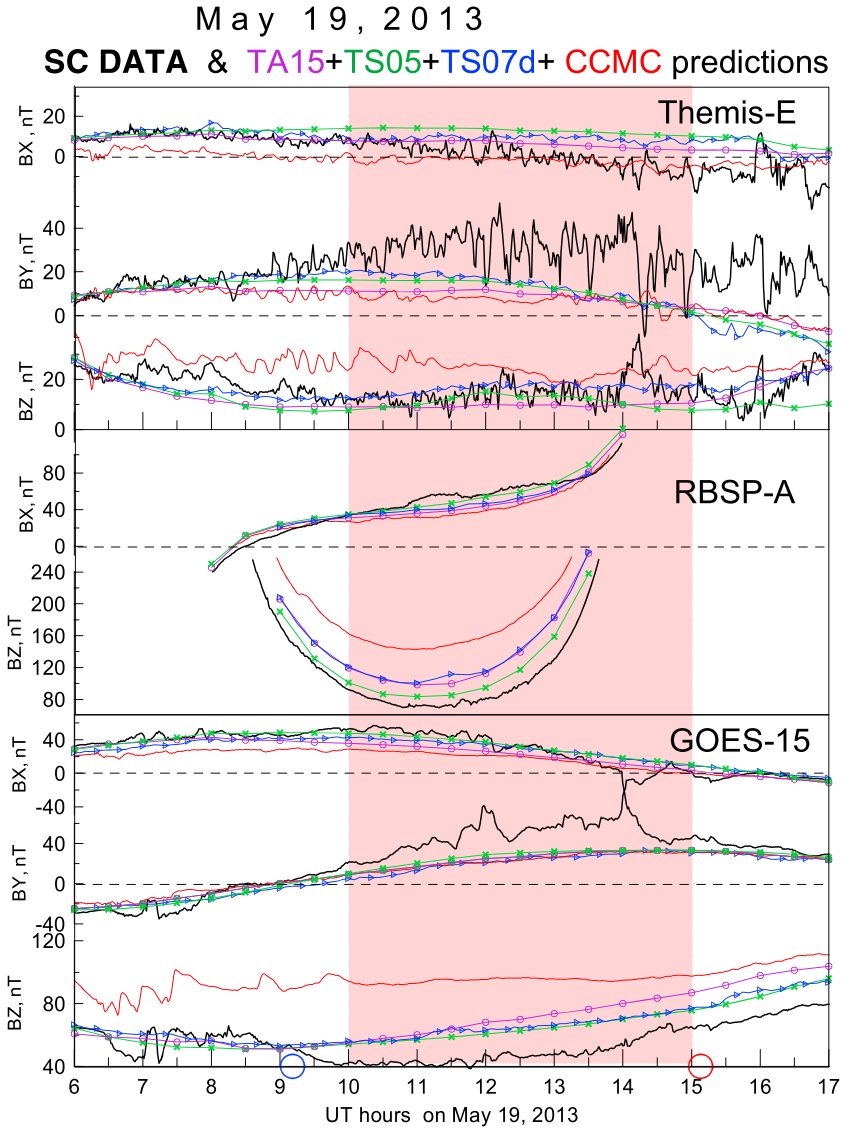

Figure 9. Comparison of SM magnetic field component observations with predictions from a GMHD simulation (red curves) and the TS05 (green), TS07d (blue), and TA15 (pink) empirical models. See text for details.

convection phase. Similarly, without accurately considering the time history and imposing the long duration requirement, the *nearest neighbor* approach to data selection in Stephens et al. (2013) most likely collected data points from different dynamical modes. The noisy data set and uneven sampling of data points could result in the variable Bz(*r*) profiles demonstrated by these authors, for example, those with or without Bz minima or with Bz minima at different distances. The above factors along with strongly fluctuating Bz in the dipolarized plasma sheet, combined with the generally small total number of SMC events, are currently the major obstacles to empirical modeling of SMC events.

A big problem with SMC identification concerns the observational tools and algorithms used to deselect substorm-like activations. The attractive, simple AL-index-based procedure used in most recent studies (following O'Brien et al., 2002, see also Kissinger et al., 2010), is rather subjective and severely limited. In particular, it may miss real activations as well as provide false alarms; both cases are represented in our event. For example, a global Pi2 burst at 1510 UT had no associated large variations in the AL or SML indices (Figure 2) and would not be identified as a substorm activation from use of the AL index alone. The SuperMAG-based substorm onset identification algorithm (Newell & Gjerloev, 2011), on the other hand, provided onsets at 0639, 1101, 1144, 1221, and 1353 UT. Of these, the first was a true substorm onset, consistent

with Pi2 and energetic particle injections (Figures 2 and 3) and identified at a near-midnight station. The other four intervals fell into the middle of the SMC period; all these onsets were identified by a station located under the poleward half of the auroral oval near the dawn terminator (at 05–06 hr MLT), an unusual location for substorm activation. Inspection of the magnetograms in this region indicates persistent strong variations of *H* and (the more significant) *D* components; some of these variations were recognized by the algorithm as onsets. Strong magnetic fluctuations have been previously noticed in the SMC event presented by Yahnin et al. (1994), although the largest perturbations in their case were observed in the premidnight poleward part of the oval. In our case such strong ground magnetic variations were recorded at a location nearly conjugate to the region of highly variable magnetic field in the equatorial magnetotail at $r \sim 11\ R_E$ sampled by THEMIS spacecraft (Figure 5).

4.3. SMC Modeling Challenge

For this event, predictions made by a few available empirical magnetospheric models driven by concurrent solar wind data were tested by comparing them with in situ observations. A summary of these comparisons is shown in Figure 9 for three representative spacecraft, including GOES-15 and RBSP-A in the inner magnetosphere and THEMIS-E in the equatorial return convection region at $r \sim 11\ R_E$ near the dawn terminator. Three recent empirical models (TS05, TS07D, and TA15) provide fairly similar magnetic field predictions. Between 10 and 15 UT (hatched area in Figure 9), all of them fail to capture a significant positive BY component seen at ThE and GOES-15 spacecraft in the predawn local time sector, with the difference being as large as ~30 nT. Similarly, all models significantly underestimate the BZ component depression in the nightside sector of inner magnetosphere (at GOES and RBSP-A) by as much as ~20–30 nT. The global LFM simulation also fails to predict these two features; in addition, it provides the most dipole-like configuration of the inner magnetosphere, with the simulated BZ being above the empirical model prediction by~20–40 nT in the inner magnetosphere and by ~10 nT at THEMIS spacecraft. Clearly, no reliable mapping between the magnetosphere and ionosphere can be done using each of these models. The failure of all routinely available models to reproduce essential features of the magnetic configuration during an SMC event is a challenge to be addressed in future studies.

5. Conclusions

Motivated by the difference in views regarding the magnetotail configuration, consistent with steady convection in the plasma sheet, as well as with respect to the minimal time scale appropriate to identify the steady convection events (SMC), we analyzed observations during ~10 hr of strong and steady solar wind driving. Extensive information about energetic electron LC precipitation profiles obtained by a constellation of low-altitude POES spacecraft added a global perspective to support in situ spacecraft observations in the magnetotail. We found that after 3–4 hr of activity that followed the north-south IMF turning, including large-scale substorm-related reconfigurations and plasma injections, the near-Earth configuration evolved into a hybrid state and stayed in that state for more than 5 hr until the end of the event. Based on these observations we recommend setting the minimal event duration to 3 hr when attempting to investigate genuine SMC events.

A hybrid configuration is confirmed during a true SMC, which includes a distant CS-like region (contiguous to the tail reconnection separatrix and corresponding to reconnection outflow), a wide dipolarized region in the midtail (with a complicated Bz landscape in the neutral sheet, possibly formed by BBFs), and a region with enhanced stretching in the inner magnetosphere, including a CS area corresponding to a local Bz^2/j minimum near the outer boundary of the radiation belt in the nightside magnetotail. The latter feature was absent during the substorm stage but was observed during the entire steady convection stage. Such a Bz^2/j minimum may be an important factor that allows steady flow-through convection to reach the inner region. In the low-altitude observations the hybrid configuration is manifested as a region of nearly empty LC filling sandwiched between two regions of isotropic LC electron precipitation, one located near the PCB and another one near the radiation belt outer boundary.

The observation of a hybrid configuration during a long-duration SMC event provides a challenge for researches, because such configurations are not yet adequately reproduced by existing global MHD or empirical magnetospheric models.

Acknowledgments

This research was supported by the Russian Science Foundation grant 14-17-00072. We thank all data providers who made available the spacecraft and ground observations used in this study. The POES and ACE spacecraft observations (in OMNI database) as well as GOES particle data and THEMIS and RBSP-A observations have been made available via CDAWeb site (http://cdaweb.gsfc.nasa.gov). The GOES magnetic field observations are available from NOAA/NGDC website (https://www.ngdc.noaa.gov/stp/satellite/goes/). The Wp index is available at WDC-C website http://wdc.kugi.kyoto-u.ac.jp/wdc/Sec3.html. The APL/JHU websites provided the SuperMAG data (from http://supermag.jhuapl.edu/), the information about DMSP boundaries (from http://sd-www.jhuapl.edu/Aurora/), and information about SSUSI DMSP auroral observations. Global MHD simulations using LFM model have been performed at NASA CCMC; the simulation results are available at https://ccmc.gsfc.nasa.gov (run Victor_Sergeev_042717_1). We thank V. G. Merkin and M. I. Sitnov for valuable discussions and Judy Hohl for help in the manuscript preparation. This paper benefited from discussions during the meetings of ISSI team "Explosive Processes in the Magnetotail: Reconnection Onset and Associated Plasma Instabilities" led by Mikhail Sitnov.

References

Akasofu, S.-I. (1964). The development of the auroral substorm. *Planetary and Space Science*, *12*(4), 273–282. https://doi.org/10.1016/0032-0633(64)90151-5

Artemyev, A. V., Angelopoulos, V., Runov, A., & Petrokovich, A. (2016). Properties of current sheet thinning at X ~ −10 to −12 R_E. *Journal of Geophysical Research: Space Physics*, *121*, 6718–6731. https://doi.org/10.1002/2016JA022779

DeJong, A. D., Ridley, A. J., Cai, X., & Clauer, C. R. (2009). A statisticalstudy of BRIs (SMCs), isolated substorms, and individual saw tooth injections. *Journal of Geophysical Research*, *114*, A08215. https://doi.org/10.1029/2008JA013870

DeJong, A. D., Ridley, A. J., & Clauer, C. R. (2008). Balanced reconnection intervals: Four case studies. *Annales de Geophysique*, *26*(12), 3897–3912. https://doi.org/10.5194/angeo-26-3897-2008

Delcourt, D. C., Sauvaud, J.-A., Martin, R. F. Jr., & Moore, T. E. (1996). On the nonadiabatic precipitation of ions from the near-Earth plasma sheet. *Journal of Geophysical Research*, *101*, 17,409–17,418. https://doi.org/10.1029/96JA01006

Dmitrieva, N. P., Sergeev, V. A., & Shukhtina, M. A. (2004). Average characteristics of the midtail plasma sheet in different dynamic regimes of the magnetosphere. *Annales de Geophysique*, *22*(6), 2107–2113. https://doi.org/10.5194/angeo-22-2107-2004

Donovan, E. F., Jackel, B. J., Voronkov, I., Sotirelis, T., Creutzberg, F., & Nicholson, N. A. (2003). Ground-based optical determination of the b2i boundary: A basis for an optical MT-index. *Journal of Geophysical Research*, *108*(A3), 1115. https://doi.org/10.1029/2001JA009198

Erickson, G. M., & Wolf, R. A. (1980). Is steady convection possible in the Earth's magnetotail? *Geophysical Research Letters*, *7*, 897–900. https://doi.org/10.1029/GL007i011p00897

Evans, D. S., & Greer, M. S. (2000). Polar Orbiting Environmental Satellite Space Environment Monitor-2: Instrument descriptions and archive data documentation, *NOAA Tech. Memo., OAR SEC 93*, 93, Version 1.4, Boulder, Colo., 2004 Jan.

Gordeev, E., Sergeev, V., Merkin, V., & Kuznetsova, M. (2017). On the origin of plasma sheet reconfiguration during the substorm growth phase. *Geophysical Research Letters*, *44*, 8696–8702. https://doi.org/10.1002/2017GL074539

Hau, L.-N. (1991). Effects of steady state adiabatic convection on the configurationof the near-Earth plasma sheet: 2. *Journal of Geophysical Research*, *96*, 5591–5596. https://doi.org/10.1029/90JA02619

Hau, L.-N., Wolf, R., Voigt, G.-H., & Wu, C. (1989). Steady state magnetic field configurations for the Earth's magnetotail. *Journal of Geophysical Research*, *94*, 1303–1316. https://doi.org/10.1029/JA094iA02p01303

Holzworth, R. H., & Meng, C.-I. (1975). Mathematical representation of the auroral oval. *Geophysical Research Letters*, *2*, 377–380. https://doi.org/10.1029/GL002i009p00377

Hoshino, M., Mukai, T., Terasawa, T., & Shinohara, I. (2001). Superthermal electron acceleration in magnetic reconnection. *Journal of Geophysical Research*, *106*, 25,979–25,997. https://doi.org/10.1029/2001JA900052

Huang, C.-S., Foster, J. C., Reeves, G. D., Le, G., Frey, H. U., Pollock, C. J., et al. (2003). Periodic magnetospheric substorms: Multiple space-based and ground-based instrumental observations. *Journal of Geophysical Research*, *108*(A11), 1411. https://doi.org/10.1029/2003JA009992

Hubert, B., Gérard, J.-C., Milan, S. E., & Cowley, S. W. H. (2017). Magnetic reconnection during steady magnetospheric convection and other magnetospheric modes. *Annales de Geophysique*, *35*(3), 505–524. https://doi.org/10.5194/angeo-35-505-2017

Kissinger, J., McPherron, R. L., Angelopoulos, V., Hsu, T. S., & McFadden, J. P. (2010). An investigation of the association between steady-magnetospheric convection and CIR stream interfaces. *Geophysical Research Letters*, *37*, L04105. https://doi.org/10.1029/2009GL041541

Kissinger, J., McPherron, R. L., Hsu, T. S., & Angelopoulos, V. (2012). Diversion of plasma due to high pressure in the inner magnetosphere during steady magnetospheric convection. *Journal of Geophysical Research*, *117*, A05206. https://doi.org/10.1029/2012JA017579

Milan, S. E., Hutchinson, J., Boakes, P. D., & Hubert, B. (2009). Influences on the radius of the auroral oval. *Annales de Geophysique*, *27*(7), 2913–2924. https://doi.org/10.5194/angeo-27-2913-2009

Milan, S. E., Provan, G., & Hubert, B. (2007). Magnetic flux transport inthe Dungey cycle: A survey of dayside and nightside reconnection rates. *Journal of Geophysical Research*, *112*, A01209. https://doi.org/10.1029/2006JA011642

Newell, P. T., Feldstein, Y. I., Galperin, Y. I., & Meng, C.-I. (1996). Morphology of nightside precipitation. *Journal of Geophysical Research*, *101*, 10,737–10,748. https://doi.org/10.1029/95JA03516

Newell, P. T., & Gjerloev, J. W. (2011). Evaluation of SuperMAG auroral electrojet indices as indicators of substorms and auroral power. *Journal of Geophysical Research*, *116*, A12211. https://doi.org/10.1029/2011JA016779

Newell, P. T., Sergeev, V. A., Bikkuzina, G. R., & Wing, S. (1998). Characterizing the state of the magnetosphere: Testing the ion precipitation maxima latitude (b2i) and the ion isotropy boundary. *Journal of Geophysical Research*, *103*, 4739–4745. https://doi.org/10.1029/97JA03622

Nosé, M., Iyemori, T., Wang, L., Hitchman, A., Matzka, J., Feller, M., et al. (2012). Wp index: A new substorm index derived from high-resolution geomagnetic field data at low latitude. *Space Weather*, *10*, S08002. https://doi.org/10.1029/2012SW000785

O'Brien, T. P., Thompson, S. M., & McPherron, R. L. (2002). Steady magnetosphericconvection: Statistical signatures in the solar wind and AE. *Geophysical Research Letters*, *29*(7), 1130. https://doi.org/10.1029/2001GL014641

Pulkkinen, T. I., Partamies, N., Kissinger, J., McPherron, R. L., Glassmeier, K.-H., & Carlson, C. (2013). Plasma sheet magnetic fields and flows during steady magnetospheric convection events. *Journal of Geophysical Research: Space Physics*, *118*, 6136–6144. https://doi.org/10.1002/jgra.50574

Pytte, T., McPherron, R. L., & Hones, E. W. Jr. (1978). Multiple-satellitestudies of magnetospheric substorms: Distinction between polar magneticsubstorms and convection-driven negative bays. *Journal of Geophysical Research*, *83*, 663–679. https://doi.org/10.1029/JA083iA02p00663

Rong, Z. J., Wan, W. X., Shen, C., Petrukovich, A. A., Baumjohann, W., Dunlop, M. W., et al. (2014). Radial distribution of magnetic field in Earth magnetotail current sheet. *Planetary and Space Science*, *103*, 273–285. https://doi.org/10.1016/j.pss.2014.07.014

Sergeev, V., Nishimura, Y., Kubyshkina, M., Angelopoulos, V., Nakamura, R., & Singer, H. (2012). Magnetospheric location of the equatorward prebreakup arc. *Journal of Geophysical Research*, *117*, A01212. https://doi.org/10.1029/2011JA017154

Sergeev, V.-A. (1977). On the state of the magnetosphere during prolonged periods of the southward oriented IMF. *Physics of Solar-Terrestrial Postdam*, *5*, 39.

Sergeev, V. A., Gordeev, E. I., Merkin, V. G., & Sitnov, M. I. (2018). Does a local B-minimum appear in the tail current sheet during a substorm growth phase? *Geophysical Research Letters*, *45*, 2566–2573. https://doi.org/10.1002/2018GL077183

Sergeev, V. A., Kubyshkina, M. V., Liou, K., Newell, P. T., Parks, G., Nakamura, R., et al. (2001). Substorm and convection bay compared: Auroral and magnetotail dynamics during convection bay. *Journal of Geophysical Research*, *106*, 18,843–18,855. https://doi.org/10.1029/2000JA900087

Sergeev, V. A., Malkov, M., & Mursula, K. (1993). Testing the isotropic boundary algorithm method to evaluate the magnetic field configuration in the tail. *Journal of Geophysical Research*, *98*, 7609–7620. https://doi.org/10.1029/92JA02587

Sergeev, V. A., Pellinen, R. J., & Pulkkinen, T. I. (1996). Steady magnetospheric convection: A review of recent results. *Space Science Reviews*, *75*(3–4), 551–604. https://doi.org/10.1007/BF00833344

Sergeev, V. A., Pulkkinen, T. I., Pellinen, R. J., & Tsyganenko, N. A. (1994). Hybrid state of the tail magnetic configuration during steady convectionevents. *Journal of Geophysical Research*, *99*, 23,571–23,582. https://doi.org/10.1029/94JA01980

Sergeev, V. A., & Tsyganenko, N. A. (1982). Energetic particle losses and trapping boundaries as deduced from calculations with a realistic magnetic field model. *Planetary and Space Science*, *30*(10), 999–1006. https://doi.org/10.1016/0032-0633(82)90149-0

Sitnov, M. I., Tsyganenko, N. A., Ukhorskiy, A. Y., & Brandt, P. C. (2008). Dynamical data-based modeling of the stormtime geomagnetic field with enhanced spatial resolution. *Journal of Geophysical Research*, *113*, A07218. https://doi.org/10.1029/2007JA013003

Stephens, G. K., Sitnov, M. I., Kissinger, J., Tsyganenko, N. A., McPherron, R. L., Korth, H., et al. (2013). Empirical reconstruction of storm time steady magnetospheric convection events. *Journal of Geophysical Research: Space Physics*, *118*, 6434–6456. https://doi.org/10.1002/jgra.50592

Stephens, G. K., Sitnov, M. I., Korth, H., Gkioulidou, M., Ukhorskiy, A. Y., & Merkin, V. G. (2017). Multiscale empirical modeling of the geomagnetic field: From storms to substorms, Fall AGU Meeting, Dec 11–15, New Orleans, LA, Abstract # SM32B-04.

Tsyganenko, N. A., & Andreeva, V. A. (2015). A forecasting model of the magnetosphere driven by an optimal solar wind coupling function. *Journal of Geophysical Research: Space Physics*, *120*, 8401–8425. https://doi.org/10.1002/2015JA021641

Tsyganenko, N. A., & Sitnov, M. I. (2005). Modeling the dynamics of the inner magnetosphere during strong geomagnetic storms. *Journal of Geophysical Research*, *110*, A03208. https://doi.org/10.1029/2004JA010798

Tsyganenko, N. A., & Sitnov, M. I. (2007). Magnetospheric configurations from a high-resolution data-based magnetic field model. *Journal of Geophysical Research*, *112*, A06225. https://doi.org/10.1029/2007JA012260

Varsani, A., Nakamura, R., Sergeev, V. A., Baumjohann, W., Owen, C. J., Petrukovich, A. A., et al. (2017). Simultaneous remote observations ofintense reconnection effects by DMSP and MMS spacecraft during a stormtime substorm. *Journal of Geophysical Research: Space Physics*, *122*, 10,891–10,909. https://doi.org/10.1002/2017JA024547

Walach, M.-T., & Milan, S. E. (2015). Are steady magnetospheric convection events prolonged substorms? *Journal of Geophysical Research: Space Physics*, *120*, 1751–1758. https://doi.org/10.1002/2014JA020631

Yahnin, A., Malkov, M. V., Sergeev, V. A., Pellinen, R. J., Aulamo, O., Vennergstrom, S., et al. (1994). Features of steadymagnetospheric convection. *Journal of Geophysical Research*, *99*, 4039–4051. https://doi.org/10.1029/93JA02868

Yang, J., Toffoletto, F. R., Xing, X., & Angelopoulos, V. (2012). RCM-E simulation of the 13 March 2009 steadymagnetospheric convection event. *Journal of Geophysical Research*, *117*, A03224. https://doi.org/10.1029/2011JA017245

Yushkov, E. V., Artemyev, A. V., Petrukovich, A. A., & Nakamura, R. (2016). Current sheet flapping in the near-Earth magnetotail: Peculiarities of propagation and parallel currents. *Annales de Geophysique*, *34*(9), 739–750. https://doi.org/10.5194/angeo-34-739-2016

Zelenyi, L. M., Kovrazhkin, R. A., & Bosqued, J. M. (1990). Velocitydispersedion beams in the nightside auroral zone: AUREOL-3 observations. *Journal of Geophysical Research*, *95*, 12,119–12,139. https://doi.org/10.1029/JA095IA08P12119